

On the dewetting of liquefied metal nanostructures

Shahriar Afkhami · Lou Kondic

Received: 11 June 2013 / Accepted: 23 December 2013 / Published online: 13 February 2014
© Springer Science+Business Media Dordrecht 2014

Abstract Direct numerical simulations of liquefied metal nanostructures dewetting a substrate are carried out. Full three-dimensional Navier–Stokes equations are solved and a volume-of-fluid method is used for tracking and locating the interface. Substrate wettability is varied to study the influence of the solid–liquid interaction. The effects of initial geometry on the retraction dynamics is numerically investigated. It is shown that the dewetting velocity increases with increases in the contact angle and that the retraction dynamics is governed by an elaborate interplay of initial geometry, inertial and capillary forces, and the dewetting phenomena. Numerical results are presented for the dewetting of nanoscale Cu and Au liquefied structures on a substrate.

Keywords Dewetting · Liquefied metal nanostructures · Navier–Stokes · Surface tension · Volume-of-fluid

1 Introduction

The modeling of nanoscale fluid problems involves considering a number of issues, in particular when free boundaries are involved. This modeling is further complicated in setups involving fluid/solid interfaces. One member of a family of problems where these effects are relevant involves the evolution of liquefied metals. Very recently, these materials have been extensively considered for synthesis and assembly on the nanoscale (e.g., [1–3]). The dewetting of liquefied gold (Au) nanoparticles was experimentally considered by Habenicht and coauthors [1,2], for example. In these physical experiments, the long time dynamics of the nanodroplet is governed by the competition of the inertial, capillary, and surface forces, giving rise to droplet contraction toward a global energy minimizer; if the inertial forces overcome the adhesion energy and dissipative losses, the nanodroplet is ejected from the substrate on a time scale of the order of 10 ns. The small length and short time scales involved in this process make the experimental study of dewetting dynamics a daunting task.

Discrete molecular dynamics (MD) approaches can be utilized to simulate systems at the nanoscale [4,5]. Fuentes-Cabrera et al. [4], for example, carried out MD simulation using a Lennard-Jones (LJ) interface potential to study various wetting regimes of nanoscale liquefied copper (Cu) nanodisks on graphite. They showed that

S. Afkhami (✉) · L. Kondic
Department of Mathematical Sciences, New Jersey Institute of Technology, Newark, NJ 07102, USA
e-mail: shahriar.afkhami@njit.edu

L. Kondic
e-mail: kondic@njit.edu

the dewetting velocities were consistent with inertial flow estimates and that thicker and smaller radius nanodisks had proportionally lower velocities. They also found that for a particular choice of the LJ potential, the dewetting nanoparticles jump off from the graphite substrate at velocities that are similar to those observed experimentally in [1] for Au liquefied nanostructures on glass.

While the MD approach is very powerful, it is computationally expensive. An alternative approach is to use continuum modeling, although it is unclear that the assumptions of continuum fluid mechanics are satisfied on these very short spatial and temporal scales. In addition to concerns related to the validity of continuum models at the nanoscale, the modeling of fluid structures on substrates involves an additional degree of complexity since one needs to carefully include the liquid–solid interaction forces, which may be dominant on such short length scales. Time-dependent evolution necessarily involves a consideration of contact lines, where liquid, solid, and gas phases meet. Modeling of the physics in the vicinity of contact lines is demanding and challenging due to well-known issues related to the so-called contact line singularity [6, 7]. Due to all these complexities, typically the problem is considered within the long-wave theory, although in the context of liquid metal films this approach is questionable due to the large contact angles involved. Despite the concerns about its validity, this approach has turned out to be very useful, providing significant insight into the dynamics and stability properties of fluids at the nanoscale, including liquefied metals [8–10].

An important property of numerical schemes that must be developed for Navier–Stokes (NS) equations at the nanoscale is the ability to accurately and robustly deal with the fluid–fluid as well as fluid–solid interactions. Furthermore, capillary forces are often very important at the nanoscale, and therefore the efficacy of a numerical scheme is highly dependent on the ability of both the surface tension discretization and the flow solver to minimize the introduction and amplification of errors. Accurate computation of the geometrical properties of an interface, such as interfacial normals and curvature, sharp surface force representation, and accurate and stable simulation, is a key ingredient in feasible computation at the nanoscale. Here we use the volume-of-fluid (VoF) interface capturing methodology, which is a widespread approach to representing fluid interfaces and, when coupled to a flow solver, is also used to compute quantities related to surface tension that enter the flow calculation. Until recently, however, the VoF method was not generally deemed appropriate for the study of phenomena in which surface tension is the driving force (e.g., the wetting and dewetting of solid surfaces, as occurs in droplet and spray technologies as well as in various natural phenomena). However, recent improvements in calculating curvature and applying the surface tension force appear to have resolved this issue [11–13].

In this paper, we use numerical simulations based on full three-dimensional (3D) NS equations using a VoF method to study the dewetting of liquefied nanosized structures on substrates with varying wettability. The motion of the fluid both inside the drop and in the surrounding flow is numerically modeled. Unlike in most other theoretical and computational studies, here the Reynolds number and the contact angle need not be small. In this work, we explore whether our continuum formulation will result in simulations consistent with MD simulations using LJ potentials. We initially focus our simulations on the dewetting behavior of liquid Cu nanodisks and ring-shaped nanostructures. We then consider Au triangular nanostructures, which do not possess radial symmetry.

2 Mathematical model

The equations of conservation of mass and momentum (NS equations),

$$\nabla \cdot \mathbf{u} = 0, \quad (1a)$$

$$\frac{D(\rho \mathbf{u})}{Dt} = \nabla \cdot (-p\mathbb{I} + \tilde{\tau}) + \mathbf{F}_{st}, \quad (1b)$$

govern the fluid motion in the drop and the surrounding gas. Here \mathbf{u} is the velocity vector, p pressure, ρ fluid density, $\tilde{\tau} = \mu(\nabla \mathbf{u} + \nabla \mathbf{u}^T)$ the viscous stress tensor, where μ is the fluid dynamic viscosity, and \mathbf{F}_{st} the surface tension force (per unit volume). The flow equations are written in an Eulerian frame of reference, and thus a solution of these equations must be coupled with a methodology for following the deforming fluid–fluid interface. Here, the VoF volume-tracking algorithm is implemented [12, 14, 15]. Volume tracking requires the introduction of a scalar

function f , defined as $f = 1$ inside the drop and $f = 0$ outside the drop, for a two-fluid system. Since f is passively advected with the flow, it satisfies the advection equation

$$\frac{Df}{Dt} = 0. \quad (2)$$

Density and viscosity are then evaluated via volume-weighted formulae as

$$\rho = \rho_g + (\rho_d - \rho_g)f, \quad (3a)$$

$$\mu = \mu_g + (\mu_d - \mu_g)f, \quad (3b)$$

where subscripts d and g refer to the drop and gas phases, respectively. Surface tension is reformulated as an equivalent volume force as originally proposed in the continuum surface force (CSF) model [16] as $\mathbf{F}_{st} = \sigma \kappa \delta_S \mathbf{n}$, where σ is a constant interfacial tension, and δ_S denotes the Dirac delta function for the surface separating the fluids. The curvature κ and unit normal \mathbf{n} are geometric characteristics of the surface and are described in terms of f and computed with a second-order height-function (HF) method [11, 17–19]. If partial slip is allowed at the contact line, we will impose the Navier-slip boundary condition at the (static) solid surface $y = 0$:

$$(u, w) \Big|_{y=0} = \lambda \frac{\partial(u, w)}{\partial y} \Big|_{y=0}, \quad (4)$$

where λ is the slip length.

To investigate the effects of the relevant dimensionless parameter, we nondimensionalize the governing equations using a velocity scale $V = \sqrt{\sigma/(\rho L)}$, where L is the appropriate length scale. The resulting time scale, $T = \sqrt{\rho L^3/\sigma}$, is proportional to the time it takes for the capillary wave to propagate across the drop. With these choices of scales, the NS equations can now be written in nondimensional form:

$$\frac{D(\rho \mathbf{u})}{Dt} = \nabla \cdot (-p \mathbb{I} + \text{Oh}^{-1} \tilde{\tau}) + \mathbf{F}_{st}. \quad (5)$$

Here $\text{Oh} = \eta/\sqrt{\rho \sigma L}$ is the Ohnesorge number, representing the ratio of the time it takes for momentum to diffuse across the droplet to the period of the capillary wave.

3 Numerical model

A complete description of the numerical methodologies can be found in [11, 12, 20]. Our in-house code is built based on an early version of the open-source flow solver GERRIS (see [20]). Briefly, the domain is discretized adaptively using oct-tree finite volumes arranged hierarchically (Fig. 1). Primitive variables are collocated at cell

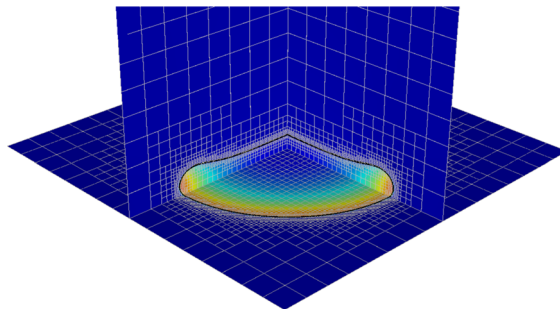


Fig. 1 Adaptive mesh: the mesh is adaptively refined around the contact line (solid line) and areas of high capillary pressure. Color contours depict the pressure distribution colored according to the reference pressure in the gas phase, with a maximum value colored in dark red and a minimum value colored in dark blue. (Color figure online)

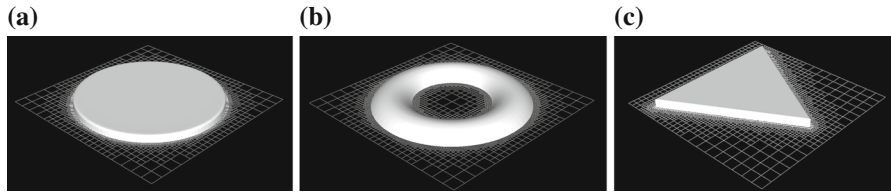


Fig. 2 Initial structures: **a** disk, **b** ring, and **c** triangular liquid nanostructures deposited on a substrate. Initial contact angle $\theta_0 = 90^\circ$ (**a**, **c**), and 60° (**b**). The computational box is 375 \AA for (**a**, **b**) and 494 nm for (**c**)

centers; normal velocities are also specified at faces, as in the marker and cell (MAC) grid. The flow equations are discretized using a projection method based on a fractional-step scheme. In the fractional-step projection method, an interim velocity is computed first; this velocity field is projected onto a divergence-free velocity field, with the pressure field obtained as the solution of a Poisson equation. Advection terms are discretized using a second-order upwind scheme [21]. As the face-centered velocities are exactly divergence-free, the volume fractions are advected using these velocities. The numerical algorithm for the imposition of the contact angle is described in details in [12]. In this algorithm, the value of the contact angle affects the overall flow calculation in two ways: it defines the orientation of the VoF reconstruction in cells that contain the contact line and it influences the calculation of \mathbf{F}_{st} by affecting the curvature calculated in cells at and near the contact line to balance the surface tension forces on the contact line, as in Young's relation [22]

$$\sigma \cos \theta_{eq} = \sigma_{sg} - \sigma_{sl}, \quad (6)$$

where σ_{sg} and σ_{sl} are interfacial tensions for the solid–gas and solid–liquid surfaces, respectively, and θ_{eq} is the equilibrium contact angle. If the actual contact angle is out of equilibrium, the resulting mismatch in curvature generates a force, thereby driving the contact line to a configuration that satisfies Young's relation.

3.1 Computational setup

We consider three geometrical configurations. Figure 2 shows the initial configurations for the case of Cu disk (Fig. 2a), Cu ring (Fig. 2b), and Au triangular (Fig. 2c) nanostructures. We denote the disk geometry by an initial height h_0 and radius R_0 ; the ring geometry by an initial outer radius R_{out} and inner radius R_{in} ; the triangle geometry by an initial long side a , short side b , and thickness h_0 ; and the initial contact angle is denoted by θ_0 . The computational domain is $L_x \times L_y \times L_z$, and the maximum grid resolution of the adaptive mesh is denoted by Δ . For all the simulations, an open boundary condition (pressure and velocity gradient equal zero) is imposed at the top, and a symmetry boundary condition is imposed on the lateral sides. For nanodisk and nanoring liquid structures, a free-slip boundary condition is specified at the substrate in accordance with the MD simulations in [4]. For triangular nanostructures, the Navier-slip boundary condition with $\lambda = 3 \text{ nm}$ is imposed, so that the computed detachment velocities are consistent with the experimental results [1, 23]. The amount of slip of thin films dewetting different substrates may vary depending on a number of conditions (such as liquid–solid interactions, shear rate, and thermal roughness). The focus of this work, however, is not to study the effect of slip, and therefore we leave this issue for future work.

4 Results

4.1 Dewetting of Cu nanostructures

4.1.1 Nanodisks

We first consider a Cu disk of $h_0 = 15 \text{ \AA}$, $R_0 = 150 \text{ \AA}$, and $\theta_0 = 90^\circ$ when the equilibrium contact angle $\theta_{eq} = 80^\circ$ is imposed. The nanodisk dewets the substrate and collapses into a spherical cap with an equilibrium base radius

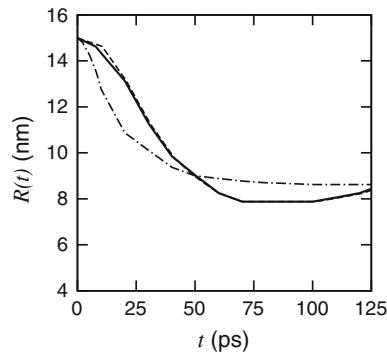


Fig. 3 Retraction of Cu nanodisk on substrate ($h_0 = 15 \text{ \AA}$, $R_0 = 150 \text{ \AA}$, $\theta_0 = 90^\circ$). Front position, $R(t)$, as a function of time for $\theta_{\text{eq}} = 80^\circ$; direct numerical simulation $\Delta = 2.93 \text{ \AA}$ (dashed line), and 1.46 \AA (solid line) for $\text{Oh} \approx 0.35$. The effect of increasing the Oh number on the retraction of the nanodisk is also plotted (continuous dotted line) for $\text{Oh} \approx 1.1$

Table 1 Overview of set of parameters used in numerical simulations [1,5]

	$\rho \text{ (kg m}^{-3}\text{)}$	$\eta \text{ (kg m}^{-1}\text{s}^{-1}\text{)}$	$\sigma \text{ (kg s}^{-2}\text{)}$	$\ell_v \text{ (nm)}$
Air	1.22	1.98×10^{-5}		
Cu	7,900	4.28×10^{-3} (at 1,500 K)	1.30	1.78
Au	17,310	4.25×10^{-3} (at 1,500 K)	1.15	0.90

$R_{\text{eq}} = 8.65 \text{ nm}$ corresponding to a contact angle of 80° . We set $L_x = L_y = L_z = 375 \text{ \AA}$. Numerical simulations are carried out on an adaptive mesh (Fig. 1) with a maximum grid resolution of $\Delta = 2.93 \text{ \AA}$. We compute the retraction of the disk and consequent coalescence into a nanodroplet. We track the position of the edge of the retracting rim $R(t)$ as a function of time. Figure 3 shows the results of direct simulations (dashed line). We also plot the simulation results with $\Delta = 1.46 \text{ \AA}$ (solid line) to show convergence with mesh refinement. After 140 ps (not shown in Fig. 3), the Cu nanodrop reaches an equilibrium state with $R_{\text{eq}} = 8.63 \text{ nm}$. The final stage is followed by contact line oscillations about the equilibrium state, a signature of inertially dominated convection. To gain additional insight regarding the effects that drive oscillations, we carried out an additional set of simulations with modified inertial effects. This was implemented by varying incompressible fluid density, but more generally the dynamics can be characterized by the Ohnesorge number, here defined as $\text{Oh} = \eta / \sqrt{\rho \sigma R_0}$. For the Cu nanodisk, $\text{Oh} \approx 0.35$, suggesting that inertial effects are important; the same conclusion can be reached by considering an intrinsic length scale, $\ell_v = \eta^2 / (\rho \sigma)$, above which inertial effects become significant; for liquid Cu, $\ell_v \approx 1.78 \text{ nm}$ (Table 1); therefore smaller than typical length scales that are considered here. As an example, we also present the computational results for $\text{Oh} \approx 1.1$ (continuous dotted line) in Fig. 3. As shown, reduced inertial effects eliminate the final stage oscillations.

Figure 4a–c shows sequences of snapshots of the simulations at various times for $\theta_{\text{eq}} = 80^\circ$, 115° , and 140° . For $\theta_{\text{eq}} = 80^\circ$, viscous forces overcome the capillary force during dewetting until the drop assumes its equilibrium shape. For $\theta_{\text{eq}} = 115^\circ$, the nanodisk quickly dewets the surface and at approximately 40 ps the retracting rim has already collapsed into a droplet that begins to elongate in the y (vertical) direction. The collapsing nanodrop then reaches a maximum elongation at around 100 ps. After that, the droplet rebounds and settles to an equilibrium state with $\theta_{\text{eq}} = 115^\circ$ at around 250 ps. In addition, the contraction in the x (horizontal) direction and the elongation in the y direction are now more pronounced compared to what was found for $\theta_{\text{eq}} = 80^\circ$. A different type of evolution occurs when θ_{eq} is increased beyond 130° . For $\theta_{\text{eq}} = 140^\circ$, the contraction is so fast that the nanodrop jumps off the surface, following elongation in the y direction. This process begins with the accumulation of the liquid material toward the center of the nanodroplet, leading to a vertical movement of the center of mass. The nanodroplet detaches from the substrate at approximately 100 ps.

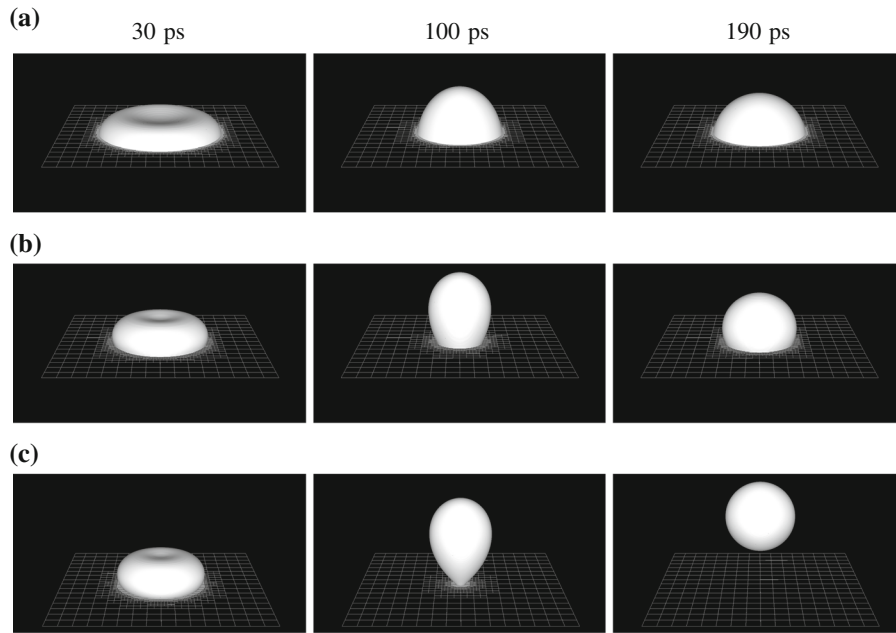


Fig. 4 Snapshots of Cu nanodisk with $h_0 = 15 \text{ \AA}$, $R_0 = 150 \text{ \AA}$, and $\theta_0 = 90^\circ$. Direct numerical simulations of NS equations for $\theta_{eq} = 80^\circ$ (a), 115° (b), and 140° (c). The computational box corresponds to 375 \AA

These continuum-based simulation results are in quantitative agreement with the MD simulations carried out in [4], suggesting that the continuum approach provides an accurate description at the scales considered. While this may appear surprising, the Cu nanodisks considered here are of a volume similar to that of a sphere with diameter corresponding to approximately 100 Cu atoms. This rather large number of atoms suggests that the continuum approach is still appropriate. Of course, precise agreement between our continuum simulations and atomistic simulations provides a much stronger argument for the appropriateness of a continuum description in the present setting.

Figure 5a–b further illustrates the relevance of inertial effects. Here we compare the x – y cross sections for the case $\theta_{eq} = 140^\circ$ where $Oh \approx 0.35$ and 1.1 . As shown, reduced inertial effects eliminate the ejection of the nanodrop from the surface. For $Oh \approx 0.35$ (Fig. 5a), a capillary ridge is formed at the initial stage and propagates from the nanodisk rim along the drop–gas interface, progressing to the top of the droplet, causing a rapid rise in the droplet height and eventual ejection, while for $Oh \approx 1.1$ (Fig. 5b), the capillary ridge is less pronounced, leading to a weaker collapse and no ejection.

We also study the effect of the equilibrium contact angle, θ_{eq} , on the retraction time and the upward velocity. Table 2 presents the variation in the retraction time and the upward velocity with θ_{eq} . As shown, the retraction dynamics is slower for smaller θ_{eq} , and the upward velocity increases with increasing θ_{eq} . These values are fully consistent with those obtained in [4] using MD simulations.

It is also instructive to compare the velocity field for various θ_{eq} . Figure 6a, b shows the velocity field, with the adaptive mesh depicted on the background, at 40 ps for $\theta_{eq} = 80^\circ$ and at 20 ps for $\theta_{eq} = 140^\circ$, respectively, where the position of the edge of the rim is the same in both cases. As shown, the magnitude of the velocities is larger for $\theta_{eq} = 140^\circ$ than the magnitude of those for $\theta_{eq} = 80^\circ$. Figure 6c, d shows the pressure field distribution corresponding to Fig. 6a, b, respectively. As described in Sect. 3, the liquid–solid interaction affects the computational results by defining the orientation of the reconstructed interface on the solid surface, which in turn influences the calculation of the curvature in cells at and near the contact line to balance the surface tension forces, resulting in a large pressure gradient there. The pressure in this region is strongly dominated by the local interfacial curvature; as shown in Fig. 6d, due to a large contact angle ($\theta_{eq} = 140^\circ$), the capillary pressure attempts to balance the difference between

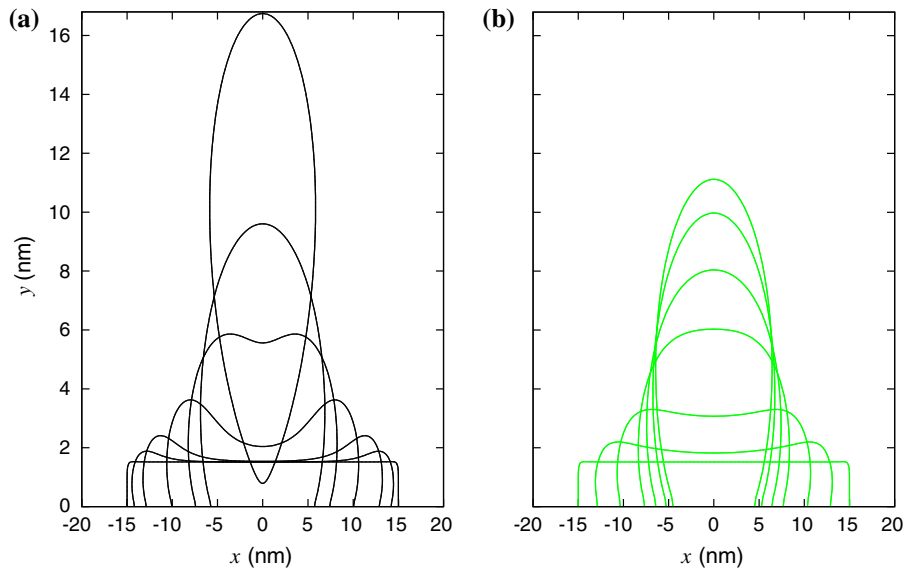


Fig. 5 x - y cross sections of a Cu disk ($h_0 = 15 \text{ \AA}$, $R_0 = 150 \text{ \AA}$, $\theta_{eq} = 140^\circ$) at $t = 0, 5, 10, 20, 30, 40, 110 \text{ ps}$ with **a** $Oh \approx 0.35$ and **b** $Oh \approx 1.1$. Case **a** results in a drop that eventually detaches from the substrate as in Fig. 4c, while for **b** the final outcome is a sessile droplet. (Color figure online)

Table 2 Effect of contact angle on retraction time and upward velocity

θ_{eq}	130°	140°	150°
Collapse time (ps)	120	100	90
Upward velocity (m s^{-1})	62	119	137

a constant pressure in the gas (dark blue contours) and the increased pressure in the liquid (dark red contours) by bending the interface. As a consequence, this leads to a thinning of the liquid in the region close to the drop center.

Figure 7 shows the front velocity, $\dot{R}(t)$, at the early time as θ_{eq} is varied. The results show a fast initial retraction followed by a slow contraction. We postulate two likely scenarios: (I) an inertially dominant regime transitions to a viscous regime and (II) the part of the kinetic energy associated with horizontal motion is transformed into that of vertical motion. We also show that the early-time inertial regime is regulated by the generation and propagation of the capillary wave initiated at the contact line (e.g., Fig. 5a). Figure 7 also shows that the contact angle condition can influence the rapid inertial flow.

4.1.2 Nanorings

We next consider the collapsing of Cu liquefied nanorings. When a ring of liquid is placed on a substrate, it retracts and collapses into a static droplet due to capillary effects [24,25]. We show here the direct computational results for the dewetting of Cu liquefied nanorings as θ_{eq} is varied. We consider the ring geometry with an initial outer radius of $R_{out} = 150 \text{ nm}$, an inner radius of $R_{in} = 75 \text{ nm}$, and $\theta_0 = 60^\circ$ (Fig. 2). The radii and the θ_0 are chosen so that the drop volume remains almost unchanged from the previous nanodisk case. The nanoring structure is out of equilibrium, and the capillary pressures resulting from the inner and outer curvature imbalance drive an inward flow that eventually leads to a collapse of the ring into a static drop. Here, $Oh \approx 0.4$ calculated based on the average radius, i.e., $(R_{out} + R_{in})/2 = 75 \text{ nm}$. We set $L_x = L_y = L_z = 375 \text{ \AA}$. Numerical simulations are carried out on an adaptive mesh (Fig. 1) with a maximum grid resolution of $\Delta = 2.93 \text{ \AA}$.

Fig. 6 Velocity vectors of Cu nanodisk dewetting ($h_0 = 15 \text{ \AA}$, $R_0 = 150 \text{ \AA}$, $\theta_0 = 90^\circ$) **a** at 20 ps for $\theta_{eq} = 80^\circ$ and **b** at 40 ps for $\theta_{eq} = 140^\circ$; the front has moved about the same distance in both cases. **c, d** Pressure field distribution colored according to reference pressure in gas phase, with a maximum value colored in *dark red* and a minimum value colored in *dark blue*, corresponding to **a** and **b**, respectively. (Color figure online)

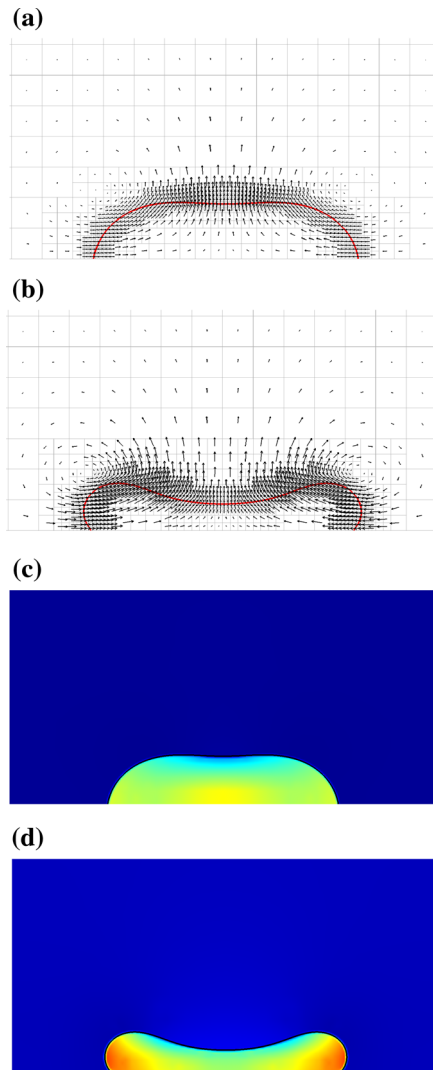


Fig. 7 Early-time retraction velocities of Cu nanodisk dewetting ($h_0 = 15 \text{ \AA}$, $R_0 = 150 \text{ \AA}$, $\theta_0 = 90^\circ$). $\theta_{eq} = 80^\circ$ (green square), 115° (blue upward-pointing triangle), 130° (black circle), and 140° (black diamond). (Color figure online)

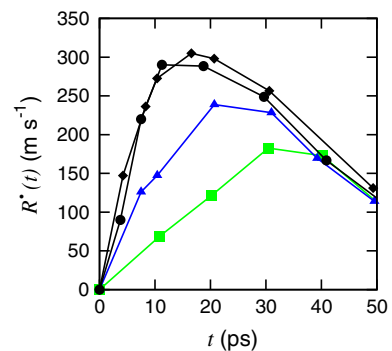


Figure 8 shows the time evolution of the nanorings for $\theta_{eq} = 45^\circ, 60^\circ, 75^\circ$, and 90° . In particular, we are interested in the time, τ , it takes for a ring to collapse, defined as the time when the inner radius goes to zero. Figure 9 shows τ as a function of θ_{eq} . We find that a larger θ_{eq} leads to a smaller collapse time. We also observe that τ scales approximately linearly with θ_{eq} .

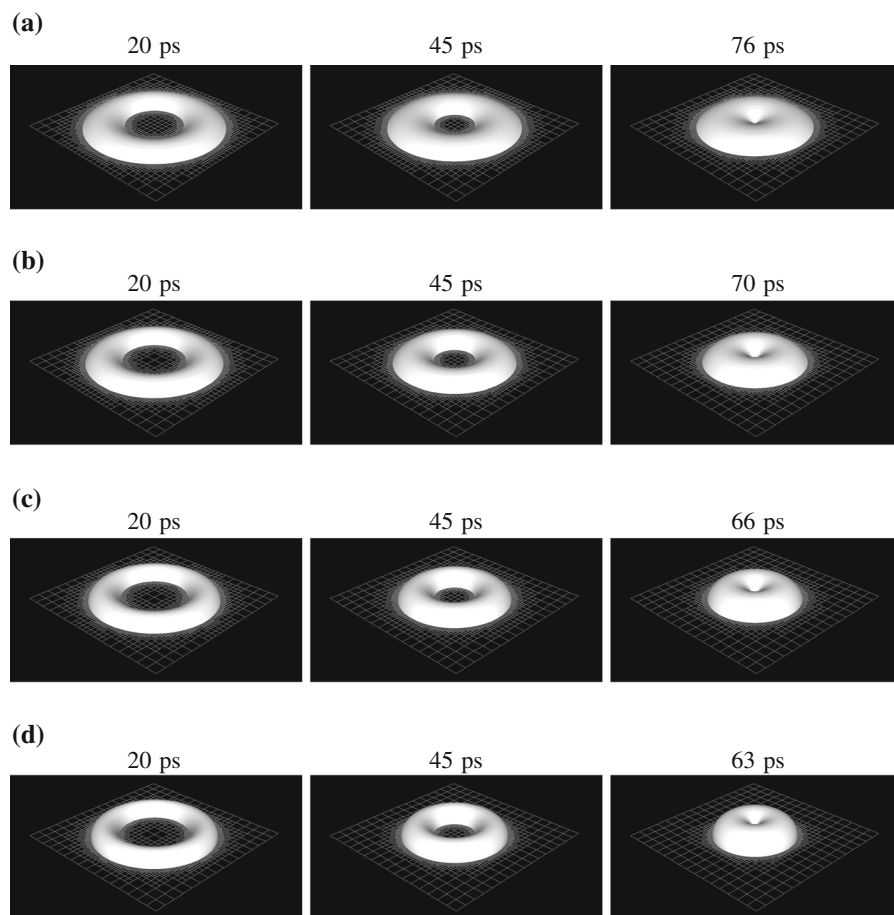


Fig. 8 Snapshots of Cu nanoring with $R_{out} = 150 \text{ \AA}$, $R_{in} = 75 \text{ \AA}$, and $\theta_0 = 60^\circ$ for $\theta_{eq} = 45^\circ$ (a), 60° (b), 75° (c), and 90° (d). The frames on the far *right* show the drop at the moment at which the collapse takes place, with the inner radius going to zero. $Oh \approx 0.4$. The computational box corresponds to 375 \AA

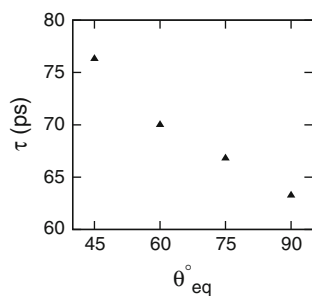


Fig. 9 Effect of θ_{eq} on collapse time, τ , for a Cu nanoring on substrate ($R_{out} = 150 \text{ \AA}$, $R_{in} = 75 \text{ \AA}$, and $\theta_0 = 60^\circ$). $Oh \approx 0.4$

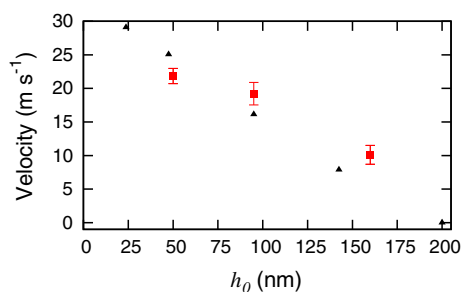


Fig. 10 Droplet detachment velocity for liquefied triangular Au nanostructures with a side length of 405 nm and various thicknesses, numerical results (black upward-pointing triangle), and experimental measurements (red square). Numerical results are obtained using a slip length of 3 nm . The numerical simulation predicts zero ejection velocity for $h_0 \geq 200 \text{ nm}$. (Color figure online)

4.2 Dewetting of Au nanostructures

4.2.1 Nanotriangles

Recently, Habenicht and coauthors [1,2] experimentally examined whether it would be possible to begin with initially deformed droplets, in the form of solid flat triangular gold structures, on the surface and observe dewetting-induced detachment. They considered Au triangular structures on the SiO₂ substrate with side lengths between 400 and 800 nm and thicknesses between 50 and 160 nm. When melted by laser irradiation, the energetically unfavorable initial structure coalesces into a droplet. The transformation of surface energy into kinetic energy drives the motion, and, under appropriate conditions, detachment of the resulting droplets was observed.

Here, we simulate the experiments of Habenicht et al. [1]. The initial triangle geometry has equal sides of $a = 405$ nm and an initial contact angle of $\theta_0 = 90^\circ$ with $\theta_{eq} = 140^\circ$ (equilibrium contact angle of liquid Au on SiO₂). The computational domain is $L_x = L_y = L_z = 494$ nm, and the maximum grid is $\Delta = 1.5$ nm. At the substrate, a Navier-slip with a slip length of 3 nm is imposed; this particular value is obtained by direct comparison with the experiments of Habenicht et al. [1]. Figure 10 represents the droplet velocity as a function of the initial thickness h_0 . Our numerical results reproduce very well the experimental findings in [1]. In particular, we note that both experiments and simulations show decreasing ejection velocity as the initial thickness is increased. This trend can be intuitively understood by realizing that the upward momentum is gained by the transformation of surface into kinetic energy. Thus, increasing the initial thickness results in a lower upward velocity by decreasing the surface-to-volume ratio. We observe that both the simulations and the experimental results show approximately the same trend for the ejection velocity as a function of h_0 , with the simulation predicting zero ejection velocity for $h_0 \geq 200$ nm.

Figure 11 shows sequences of simulations of the dewetting of initially triangular nanostructures when the initial thickness is varied. The consequent detachment of the droplet at various times is also demonstrated. As shown, the dewetting process begins at the corners, where the curvature is high. Due to a high surface tension force and large equilibrium contact angle, the liquid starts to accumulate at the corners. Vertices accumulate more mass than the straight sides. The humps at the corners then coalesce into a droplet. Finally, owing to a low viscosity of liquid gold ($\ell_v \approx 0.9$ nm; Table 1), inertia dominates over viscous dissipation, giving rise to an upward movement that leads to droplets detaching from the surface at velocities of tens of meters per second (Fig. 10). As shown, increasing the initial thickness will result in a slower dynamic and an increase in the collapsing time. The time scale of the retraction process is consistent with the experiments of Habenicht et al. [1] measuring a detachment time scale on the order of 10 ns.

Figure 12 shows the pressure distribution at the (substrate) x - z plane for $h_0 = 24$ nm (Fig. 12a) and 47 nm (Fig. 12b). The solid line represents the line of contact and the background demonstrates the adaptive grid used. The high surface tension force due to the high curvature increases the capillary pressure at the corners. This pressure gradient results in a transversal velocity driving the traveling rims. The time at which all the rims coalesce depends on the pressure gradient, explaining the difference in the collapsing times shown in Fig. 11. As is also shown, the sides of the triangle reach the center first, followed by the vertices. This asynchronicity is the reason for the excitation of the contact line oscillations during the dewetting process, as illustrated in Fig. 12.

Finally, we explore the effect of the initial shape. We consider an isosceles nanotriangle geometry with initial long side $a = 488$ nm, short side $b = 247$ nm, $h_0 = 24$ nm, $\theta_0 = 90^\circ$, and $\theta_{eq} = 145^\circ$. Figure 13a shows the sequence of the numerical results. As shown, the dewetting behavior is different compared to the dewetting dynamics of an equilateral triangle, although both processes lead to the ejection of the formed droplet from the substrate. Figure 13b shows the pressure distribution at the x - z plane. It shows a higher capillary pressure at the vertex of the long edges due to a higher curvature. However, the triangle small edge vertices arrive faster at the center than the vertex of the longer sides. This mismatch excites the oscillation of the droplet, translating into a tumbling movement after the droplet leaves the substrate.

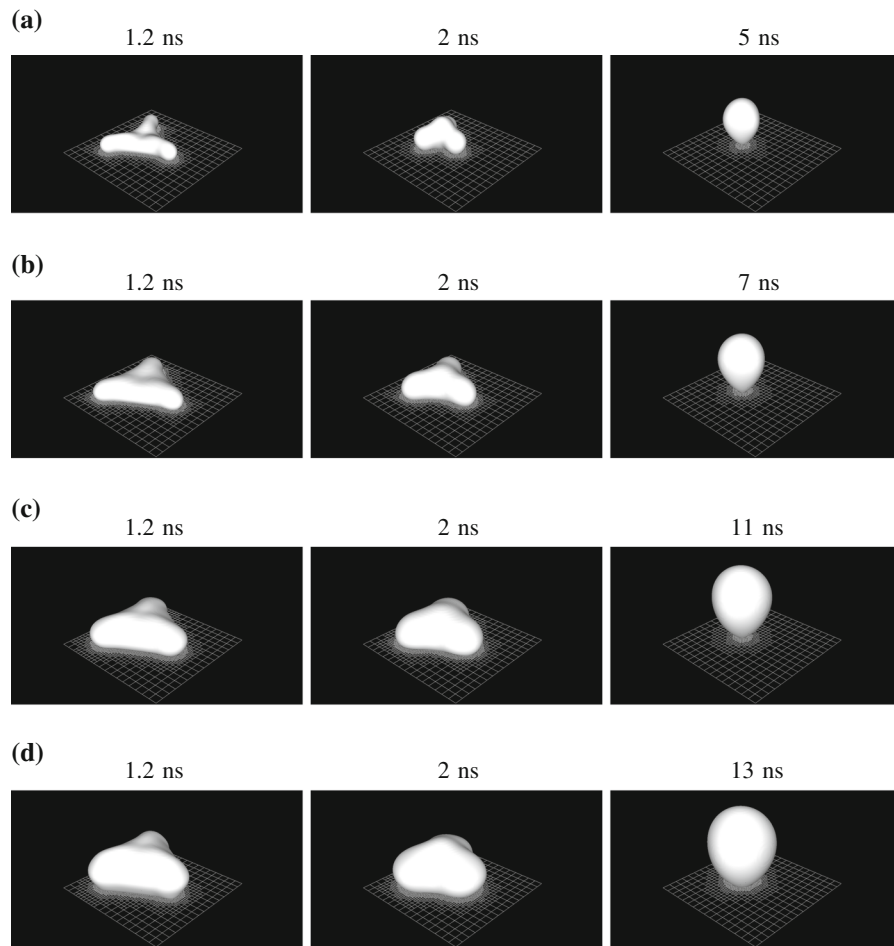


Fig. 11 Snapshots of Au equilateral nanotriangles with $a = 405$ nm, $\theta_0 = 90^\circ$, and $\theta_{eq} = 140^\circ$ for $h_0 = 24$ nm (a), 47 nm (b), 95 nm (c), and 142 nm (d). The computational box corresponds to 494 nm. The nanotriangular structure collapses into a droplet and detaches from the substrate (see Fig. 10 for corresponding ejection velocities)

5 Conclusion

We show that a direct numerical simulation based on Navier–Stokes equations can be utilized to study the dewetting of liquefied metal nanostructures. In particular, we find that the early-time dynamics of the dewetting of a Cu nanodisk is inertially dominated and that viscous dissipation cannot be expected to be the dominant resistance to short-time dewetting. Furthermore, we demonstrate that the equilibrium contact angle, θ_{eq} , plays a key role in dewetting dynamics. For sufficiently large θ_{eq} , the retraction and consequent collapse into a nanodroplet is followed by the detachment of a nanodroplet from the substrate at an upward velocity that is an increasing function of θ_{eq} . Considering Cu nanorings, we show that θ_{eq} affects the retraction velocity and the collapsing time. Our numerical results, based on a VoF formulation, are consistent with the results of MD simulations, offering a potential venue for modeling dewetting phenomena at the nanoscale. We also directly simulate the dewetting process of initially triangular Au nanostructures that coalesce into nanodroplets that, in turn, detach from the surface. We demonstrate that dewetting dynamics is consistent with experimental observations and that the computed detachment velocity is consistent with experimental measurements. We expect our findings to be of direct relevance to nanomaterial processes involving rapid dewetting.

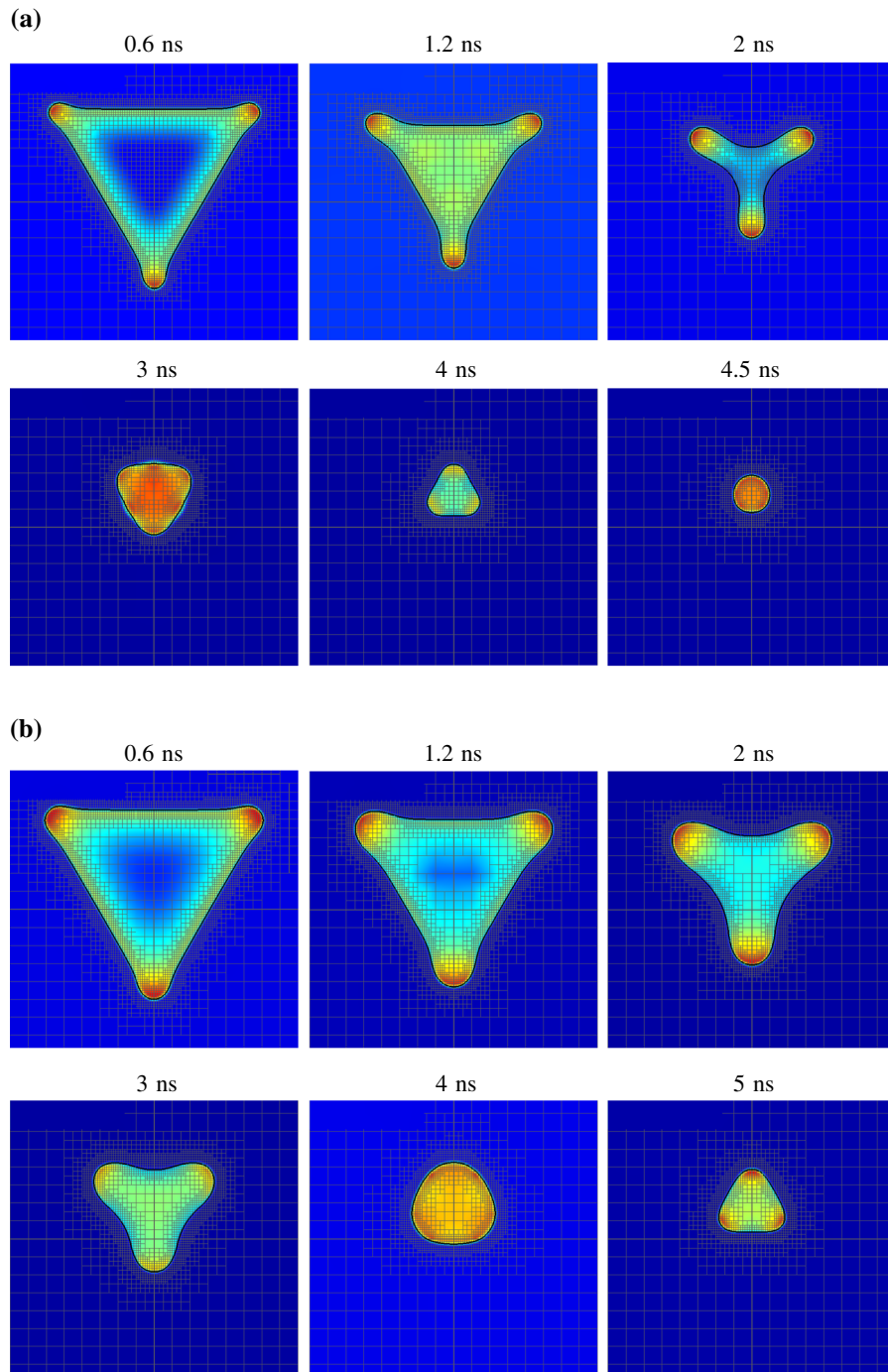


Fig. 12 Contours of pressure field distribution and adaptive mesh at x - z plane for Au equilateral nanotriangles with $a = 405$ nm, $\theta_0 = 90^\circ$, and $\theta_{eq} = 140^\circ$. **a** $h_0 = 24$ nm and **b** 47 nm. The computational box corresponds to 494 nm. The high capillary pressure at the *corners* are shown. The pressure distribution is colored according to the reference pressure in the gas phase, with maximum value colored in *dark red* and minimum value colored in *dark blue*. (Color figure online)

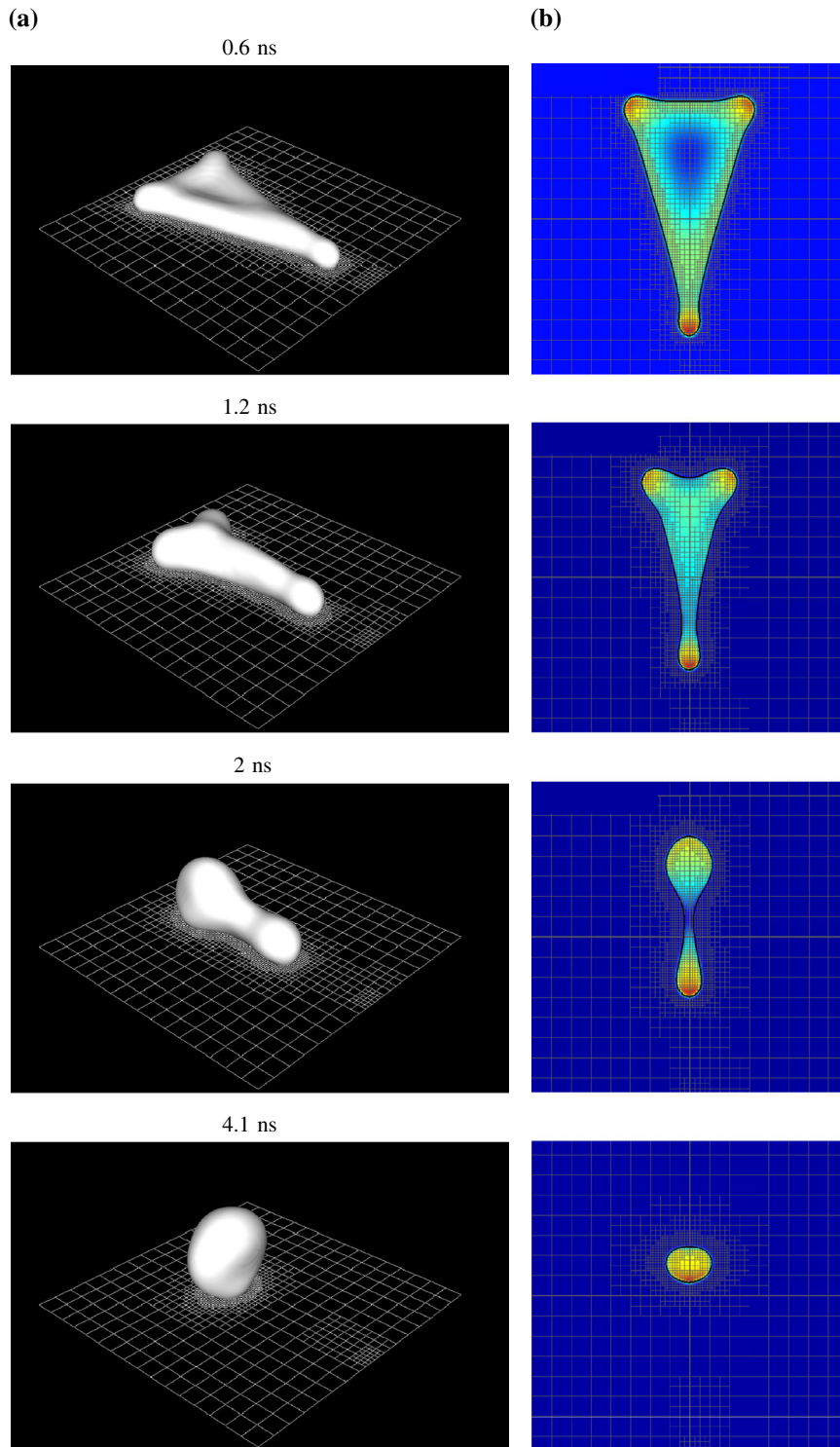


Fig. 13 **a** Snapshots of Au isosceles nanotriangle structure with $a = 488$ nm, $b = 247$ nm, $h_0 = 24$ nm, $\theta_0 = 90^\circ$, and $\theta_{eq} = 145^\circ$. The nanotriangular structure collapses into a droplet and detaches from the substrate at around 5 ns. **b** Contours of pressure field distribution and adaptive mesh at x - z plane. The computational box corresponds to 494 nm. The pressure distribution is colored according to the reference pressure in the gas phase, with maximum value colored in *dark red* and minimum value colored in *dark blue*. (Color figure online)

Acknowledgments The results presented here are a part of a larger research project involving Kyle Mahady (New Jersey Institute of Technology), Javier Diez and Alejandro Gonzalez from Universidad Nacional del Centro de la Provincia de Buenos Aires (Argentina), and Jason Fowlkes, Miguel Fuentes-Cabrera, and Philip Rack from Oak Ridge National Laboratory and the University of Tennessee. We acknowledge the extensive discussions with all members of the research team. This work was supported in part by National Science Foundation Grants DMS-1320037 (S.A.) and CBET-1235710 (L.K.).

References

1. Habenicht A, Olapinski M, Burmeister F, Leiderer P, Boneberg J (2005) Jumping nanodroplets. *Science* 309:2043
2. Boneberg J, Habenicht A, Benner D, Leiderer P, Trautvetter M, Pfahler C, Plettl A, Ziemann P (2008) Jumping nanodroplets: a new route towards metallic nano-particles. *Appl Phys A* 93:415
3. Roberts NA, Fowlkes JD, Mahady K, Afkhami S, Kondic L, Rack PD (2013) Directed assembly of one- and two-dimensional nanoparticle arrays from pulsed laser induced dewetting of square waveforms. *ACS Appl Mater Interfaces* 5:4450
4. Fuentes-Cabrera M, Rhodes BH, Fowlkes JD, López-Benzanilla A, Terrones H, Simpson ML, Rack PD (2011) Molecular dynamics study of the dewetting of copper on graphite and graphene: implications for nanoscale self-assembly. *Phys Rev E* 83:041603
5. Fuentes-Cabrera M, Rhodes BH, Baskes MI, Terrones H, Fowlkes JD, Simpson ML, Rack PD (2011) Controlling the velocity of jumping nanodroplets via their initial shape and temperature. *ACS Nano* 5:7130
6. de Gennes PG (1985) Wetting: statics and dynamics. *Rev Mod Phys* 57:827
7. Haley PJ, Miksis MJ (1991) The effect of the contact line on droplet spreading. *J Fluid Mech* 223:57
8. Trice J, Thomas D, Favazza C, Sureshkumar R, Kalyanaraman R (2007) Pulsed-laser-induced dewetting in nanoscopic metal films: theory and experiments. *Phys Rev B* 75:235439
9. Ajaev VS, Willis DA (2003) Thermocapillary flow and rupture in films of molten metal on a substrate. *Phys Fluids* 15:3144
10. Kondic L, Diez J, Rack P, Guan Y, Fowlkes J (2009) Nanoparticle assembly via the dewetting of patterned thin metal lines: understanding the instability mechanism. *Phys Rev E* 79:026302
11. Afkhami S, Bussmann M (2008) Height functions for applying contact angles to 2D VOF simulations. *Int J Numer Method Fluids* 57:453
12. Afkhami S, Bussmann M (2009) Height functions for applying contact angles to 3D VOF simulations. *Int J Numer Method Fluids* 61:827
13. Afkhami S, Zaleski S, Bussmann M (2009) A mesh-dependent model for applying dynamic contact angles to VOF simulations. *J Comput Phys* 228:5370
14. Hirt CW, Nichols BD (1981) Volume of fluid VOF method for the dynamics of free boundaries. *J Comput Phys* 39:201
15. Gueyffier D, Li J, Nadim A, Scardovelli R, Zaleski S (1999) Volume-of-fluid interface tracking and smoothed surface stress methods for three-dimensional flows. *J Comput Phys* 152:423
16. Brackbill JU, Kothe DB, Zemach C (1992) A continuum method for modeling surface tension. *J Comput Phys* 100:335
17. Sussman M (2003) A second order coupled level set and volume-of-fluid method for computing growth and collapse of vapor bubbles. *J Comput Phys* 187:110
18. Cummins SJ, Francois MM, Kothe DB (2005) Estimating curvature from volume fractions. *Comput Struct* 83:425
19. Francois MM, Cummins SJ, Dendy ED, Kothe DB, Sicilian JM, Williams MW (2006) A balanced-force algorithm for continuous and sharp interfacial surface tension models within a volume tracking framework. *J Comput Phys* 213:141
20. Popinet S (2003) Gerris: a tree-based adaptive solver for the incompressible Euler equations in complex geometries. *J Comput Phys* 190:572
21. Bell JB, Colella P, Glaz HM (1989) A second-order projection method for the incompressible Navier–Stokes equations. *J Comput Phys* 85:257
22. Young T (1805) An essay on the cohesion of fluids. *Philos Trans R Soc Lond* 95:65–87
23. Afkhami S, Kondic L (2013) Numerical simulation of ejected molten metal nanoparticles liquified by laser irradiation: interplay of geometry and dewetting. *Phys Rev Lett* 111:034501
24. González AG, Diez JA, Kondic L (2013) Stability of a liquid ring on a substrate. *J Fluid Mech* 718:246
25. Mahady K, Afkhami S, Diez J, Kondic L (2013) Comparison of Navier–Stokes simulations with long-wave theory: study of wetting and dewetting. *Phys Fluids* 25:112103